Applied Surface Science 720 (2026) 165240

Contents lists available at ScienceDirect

Applied Surface Science

journal homepage: www.elsevier.com/locate/apsusc

Full Length Article

Br/I gradient-engineered $CsPbX_3$ nanosheets: polymer-encapsulated design for polarized X-ray radioluminescence

Zhibin Xu [a], Zhiheng Xu [a,b,*], Sirui Zhu [a], Xuebin Zhang [a], Dandan Yang [c], Xiaobin Tang [a,b,**]

[a] Department of Nuclear Science and Technology, Nanjing University of Aeronautics and Astronautics, Nanjing 211106, China
[b] Key Laboratory of Advanced Nuclear Technology and Radiation Protection, Ministry of Industry and Information Technology, Nanjing 211106, China
[c] Institute of Innovation Materials and Energy, School of Chemistry and Chemical Engineering, Yangzhou University, Yangzhou 225002, China

ARTICLE INFO

Keywords:
$CsPbX_3$
Perovskite nanosheets
X-ray excitation
Radiation-induced polarized emission
Optical anisotropy regulation

ABSTRACT

Two-dimensional $CsPbX_3$ perovskite nanosheets serve as unique platforms for polarized emission modulation. However, the integrated control mechanism of bandgap engineering and polarized optical properties remains largely unexplored. In this study, we demonstrated a halogen gradient strategy using iodine-doped $CsPbBr_{3-x}I_x$ nanosheets with polymer encapsulation, enabling simultaneous band structure modification and optical anisotropy regulation. The iodine gradient enabled continuous tuning of the degree of polarization (up to 0.39) across a broad-spectrum range of 520–677 nm. Notably, radiation-induced polarized emission was observed in perovskite nanostructures under X-ray excitation, revealing directional transport behavior under high-energy stimulation. This work presents a detailed systematic investigation into X-ray-induced linearly polarized luminescence from perovskite nanosheets. The polarization-sensitive response detector exhibited enhanced current ratios, which can be attributed to iodine-induced defect suppression. This work not only advances the field of polarized optoelectronics but also establishes new opportunities for the detection of X-ray polarization response.

1. Introduction

In recent years, lead halide perovskite nanocrystals (NCs) have emerged as a subject of in-depth research in the field of materials science owing to their unique structural and optoelectronic properties [1–3]. The anisotropic structures (quantum dots (QDs), nanorods (NRs), nanosheets (NSs), and nanowires (NWs)) and chiral induction mechanisms (chiral carbon dots, supramolecular assembly) exhibit significant linearly polarized and circularly polarized luminescence properties, which have broad application prospects in polarized optoelectronic devices, high-resolution displays, optical communications, quantum information encryption, and dynamic anti-counterfeiting labels [4–7]. Specifically, the formation of band-like triplet excitonic states with orthogonal polarization components governs the polarized photoluminescence emission of these materials.

While existing methods predominantly employ lasers as excitation sources for polarization modulation, the polarization dynamics remain largely uncharted under high-energy photon excitation, particularly within the X-ray spectral range. Lead halide perovskites exhibit efficient photon conversion upon exposure to high-energy X-ray photons, effectively converting the incident radiation into directionally polarized visible light. This polarized light emission mechanism induced by high-energy particles shows considerable promise for high-sensitivity X-ray response detection applications, leveraging the unique coupling between radiation excitation and anisotropic optical responses [8]. Current reports on the polarization luminescence of perovskite NCs mainly focus on the study of QDs, NWs, and supercrystals (SCs). Wang *et al.* synthesized full-inorganic $CsPbX_3$ (X = Br, I) perovskite QDs exhibiting excellent photoluminescence and highly polarized emission, demonstrating exceptional potential for low power, wide color gamut displays [2]. Li *et al.* developed highly aligned 2D layered perovskites incorporating 1D $CsPbBr_3$ NWs arrays with exceptional crystallinity and optical anisotropy, employing organic hydrophobic encapsulation to ensure environmental stability during optoelectronic characterization [9]. Meanwhile, Zhou *et al.* achieved substrate-controlled synthesis of β-$CsPbI_3$ NWs through a one-step self-assembly process on Si/SiO_2 substrates, demonstrating photocurrent anisotropy ratios up to 2.68 upon transfer to flexible polyethylene terephthalate substrates [10]. Ye *et al.* achieved direct 74.4 % linearly polarized electroluminescence from $CsPbI_3$ nanoplatelet superlattice LEDs by controlling nanocrystal

* Corresponding author at: Department of Nuclear Science and Technology, Nanjing University of Aeronautics and Astronautics, Nanjing 211106, China.
** Corresponding author at: Department of Nuclear Science and Technology, Nanjing University of Aeronautics and Astronautics, Nanjing 211106, China.
E-mail addresses: xuzhiheng@nuaa.edu.cn (Z. Xu), tangxiaobin@nuaa.edu.cn (X. Tang).

https://doi.org/10.1016/j.apsusc.2025.165240
Received 20 August 2025; Received in revised form 24 October 2025; Accepted 11 November 2025
Available online 12 November 2025

orientation via solvent vapor pressure during self-assembly. This solution-processable system enables filter-free polarized light sources for 3D displays [11]. However, current research on perovskite NS polarization has prioritized efficient circularly polarized luminescence (CPL). Wen *et al.* achieved tunable deep-blue-to-sky-blue CPL ($g_{lum} = -8.0 \times 10^{-3}$) in electrospun quasi-2D chiral perovskite NSs/polymer nanofibers, with enhanced stability from polymer encapsulation [12]. Hubley *et al.* enabled efficient CPL in $MAPbBr_3$ wvia precise chiral/non-chiral ligand ratio control, linking CPL-CD correlation to optoelectronic design [13]. Chen *et al.* demonstrated ligand-chirality-directed two-photon upconverted CPL ($g_{lum} = 7.0 \times 10^{-3}$, $\sigma_2 = 3.68 \times 10^4$ GM at 800 nm) in chiral α-methylbenzylamine-modified $CsPbBr_3$ NCs [14].

Although $CsPbX_3$ NSs have been extensively studied for their CPL properties, research on their linearly polarized luminescence and polarization-sensitive response detection remains scarce. Moreover, the synergistic modulation mechanism between bandgap engineering and the polarization characteristics of $CsPbX_3$ NS systems has rarely been documented. To address this knowledge gap, we propose a halogen gradient strategy using controlled iodine doping to synthesize $CsPbBr_{3-x}I_x$ NSs, enabling concurrent band structure modification and optical anisotropy regulation. Moreover, although previous studies have overlooked the directional carrier transport characteristics in NCs under high-energy excitation, we systematically examined the polarization-dependent luminescence behavior under X-ray irradiation [15–24]. Although polymer encapsulation has been shown to effectively enhance the stability of $CsPbX_3$ NSs, the critical correlation between the thickness of the encapsulation layer and the polarization generation efficiency remains unexplored.

In this work, we systematically investigated the polarization luminescence of anisotropic two-dimensional $CsPbBr_{3-x}I_x$ perovskite NSs, revealing their structure–property relationships. We achieved broadband polarized emission (520–677 nm) via an iodide gradient strategy using polarization performance enhancement by means of synergistic control of bandgap engineering and polarized optical properties. We demonstrated radiation-induced polarized emission under X-ray excitation, representing the systematic investigations into X-ray-induced linearly polarized luminescence from perovskite nanosheets. These findings establish the transformative potential of $CsPbX_3$ NS composite films for X-ray polarization-sensitive response detection systems and advanced polarization imaging technologies.

2. Experiment

2.1. Materials

Cesium acetate (CsAc, AR, 99 %), lead bromide ($PbBr_2$, AR, 99 %), and lead iodide (PbI_2, 98 %) were purchased from Macklin Chemicals. Propanol (1-PrOH, AR, 99 %), n-hexane (Hex, AR, 97 %), octanoic acid (OcAc, AR, 99 %), octylamine (OcAm, AR, 99 %), and polystyrene (PS) were purchased from Aladdin. Toluene (TOL) was purchased from Nanjing Reagents. All chemicals were used without further purification.

2.2. Synthesis of $CsPbX_3$ NSs

2.2.1. Synthesis of $CsPbBr_3$ NSs

The $CsPbBr_3$ NSs were synthesized through a two-step precursor reaction with a molar ratio of 4:1 (Cs: $PbBr_2$). Initially, the cesium precursor solution was prepared by completely dissolving 96 mg of cesium acetate in 3 mL of 1-propanol in a 50 mL beaker. Subsequently, 6 mL of 1-PrOH and 18 mL of hexane were sequentially added to the solution with continuous stirring. Simultaneously, the lead bromide precursor was formulated by dissolving 735 mg of $PbBr_2$ in a ternary solvent mixture containing 1.35 mL 1-PrOH, 1.35 mL OcAm, and 1.35 mL OcAc mixture. The mixture was subjected to vigorous magnetic stirring at 90 °C until a transparent homogeneous solution was obtained. The synthesis was initiated by the rapid injection of the $PbBr_2$ precursor into the cesium precursor solution, followed by 30 s of intense stirring to yield a characteristic green colloidal suspension. The resulting $CsPbBr_3$ NSs were isolated via centrifugation at 4,000 rpm for 3 min and subsequently redispersed in 2 mL of toluene via ultrasonic treatment for long-term storage.

2.2.2. Synthesis of $CsPbI_3$ NSs

$CsPbI_3$ NSs were synthesized using a controlled anion exchange protocol. First, the PbI_2 precursor solution was prepared by dissolving 924 mg of lead iodide (PbI_2) in a ternary solvent system containing 1.35 mL 1-PrOH, 1.35 mL OcAm, and 1.35 mL OcAc. The mixture was vigorously stirred at 90 °C until complete dissolution, yielding a transparent homogeneous solution. The anion exchange reaction was initiated by injecting the PbI_2 precursor solution into a pre-synthesized $CsPbBr_3$ NS colloidal solution (prepared via the method described earlier) at a predetermined stoichiometric ratio. An immediate color transition to red occurred within seconds under vigorous stirring, indicating successful halide substitution. The resultant $CsPbI_3$ NSs were isolated by centrifugation at 4000 rpm for 3 min and redispersed in toluene for further characterization. To systematically tune the halide composition (Br/I ratio), $CsPbBr_{3-x}I_x$ NSs were synthesized by adjusting the molar ratio of the PbI_2 precursor to the $CsPbBr_3$ NSs while maintaining identical processing parameters. I/Br stoichiometric control was achieved through systematic variation of the precursor feed ratios, following the same synthesis protocol.

2.3. Preparation of $CsPbX_3$ NS films

The composite film was synthesized through solution processing, and a typical preparation procedure was carried out according to the following steps. Initially, 1 g of polystyrene was dissolved in 4 mL of toluene via magnetic stirring at 60 °C until complete homogenization. Subsequently, 100 mg of $CsPbX_3$ NSs were incorporated into the polymer matrix under continuous stirring until molecular-level dispersion was achieved. The homogeneous precursor solution was deposited onto glass substrates using a doctor-blade coating technique (gap height: 250 μm) to create films with controlled thicknesses. Immediate thermal treatment at 60 °C facilitated controlled solvent evaporation, followed by a two-stage curing process: 1) vacuum-drying to remove residual solvent, and 2) thermal annealing at 45 °C for 2 h under vacuum (–0.095 MPa) to enhance polymer chain entanglement. The freestanding composite films were ultimately detached from the glass substrate by mechanical peeling for subsequent characterization.

2.4. Measurements and characterization

X-ray diffraction (XRD) analysis was performed using an Empyrean X-ray diffractometer with Cu Kα radiation (λ = 1.5406 Å). The photoluminescence (PL) and radioluminescence (RL) spectra of both $CsPbX_3$ NSs and $CsPbX_3$-embedded polymer films were recorded using an Agilent Cary Eclipse fluorescence spectrometer. The optical absorption characteristics of the perovskite materials were quantitatively evaluated using a UV–Vis-NIR spectrophotometer (OPTOSKY UV3610). The linear polarization characteristics were investigated using a JCOPTIX thin-film linear polarizer (400–700 nm spectral range), with polarization-dependent measurements conducted through systematic rotation of the polarizer orientation. Morphological characterization was achieved using field-emission high-resolution transmission electron microscopy (FE-HRTEM) for transmission electron microscopy (TEM) imaging and a LYRA3-GMU scanning electron microscope for scanning electron microscopy (SEM) analysis. The electrical output performance of the response signal in the polarization response detection was systematically evaluated under controlled irradiation conditions using a Keithley 2636A digital sourcemeter. External quantum efficiency (EQE) analysis was performed using a certified quantum efficiency measurement system (QE-R, ENLITECH) compliant with the ASTM E1021 standards.

3. Results and discussion

3.1. Preparation and characterization of $CsPbX_3$ NS films

$CsPbBr_3$ NSs were prepared at 25 °C via a room-temperature co-precipitation method using a conventional octanoic acid (OcAc)-octylamine (OcAm) ligand system. In contrast, $CsPbI_3$ NSs were fabricated using an anion displacement strategy. The thin-film preparation process is illustrated in Fig. 1a, where the NS suspension was homogeneously blended with polystyrene (PS) dissolved in toluene under vigorous magnetic stirring to facilitate the rapid diffusion of the NSs into the polymer matrix. Subsequently, a controlled volume of the resulting NS-PS colloidal dispersion was deposited on a glass substrate using a doctor blade coater. After naturally cooling to room temperature, the free-standing films were readily delaminated from their substrates. Additionally, $CsPbBr_{3-x}I_x$ NSs with different Br/I molar ratios were successfully synthesized using the same strategy (Fig. S1; Supporting Information). The fabrication process for the corresponding polymer composite films is illustrated in Fig. 1a. Specifically, the physical image of the $CsPbX_3$ NS polymer film prepared by us is shown in Fig. S2, including a comparison of luminescence under indoor light and ultraviolet (UV) light.

Notably, during the preparation of the $CsPbX_3$ NS colloidal solutions, rapid phase separation with substantial precipitation was evident within three minutes of aging. This behavior is in stark contrast to that of polymer-encapsulated composite films, which demonstrate remarkable colloidal stability over several months of storage without detectable phase separation or nanoparticle aggregation. The synergistic combination of enhanced colloidal stability and well-preserved optoelectronic characteristics endows these polymer-integrated NS systems with remarkable competitiveness in radiation-related applications. This dual advantage makes them particularly suitable for RL, radiation imaging, and X-ray response detection.

XRD analysis revealed distinct structural differences among the $CsPbBr_3$, $CsPbBr_{1.5}I_{1.5}$, and $CsPbI_3$ NS polymer films [25–28]. As shown in Fig. 1b, the characteristic diffraction peaks of the $CsPbBr_3$ NSs were evident at 28° (122) and 33° (105), whereas the $CsPbI_3$ and $CsPbBr_{1.5}I_{1.5}$ NSs exhibited discernible peak shifts at the corresponding positions. Despite the expectation of shear-induced alignment, the lack of pronounced texture in the XRD patterns indicates that any local ordering of nanosheets is obscured at the macroscopic scale. This is attributed to the confinement effect of the polymer matrix and the spatial averaging inherent to the XRD technique, which together preclude the detection of strong preferred orientation [29]. Although the macroscopic XRD measurement did not reveal a strong preferred orientation, the significant polarized emission observed in subsequent sections confirms the existence of local alignment and anisotropic optical transition dipoles within the nanosheets, which is sufficient to generate pronounced polarization-dependent luminescence. This is consistent with the HRTEM results shown in Fig. 1c and d [30,31]. These observations collectively confirmed the structural modifications arising from halide composition variations [25,27,32]. The TEM images in Fig. 1f and g show that both $CsPbBr_3$ and $CsPbI_3$ NSs displayed relatively aggregated morphologies. As shown in Fig. 1e, the PS polymer film incorporating the $CsPbBr_3$ NSs exhibited excellent phase homogeneity without nanoparticle aggregation. This indicates optimal compatibility within the matrix nanostructure and a well-matched polymer–polymer pairing between the NS and the polymer host, that prevents agglomeration [33]. Furthermore, nanosheet non-uniformity benefits surface passivation. It enhances overall luminescence intensity by promoting tighter packing in the composite film, reducing interface defects and improving light scattering to further advance passivation.

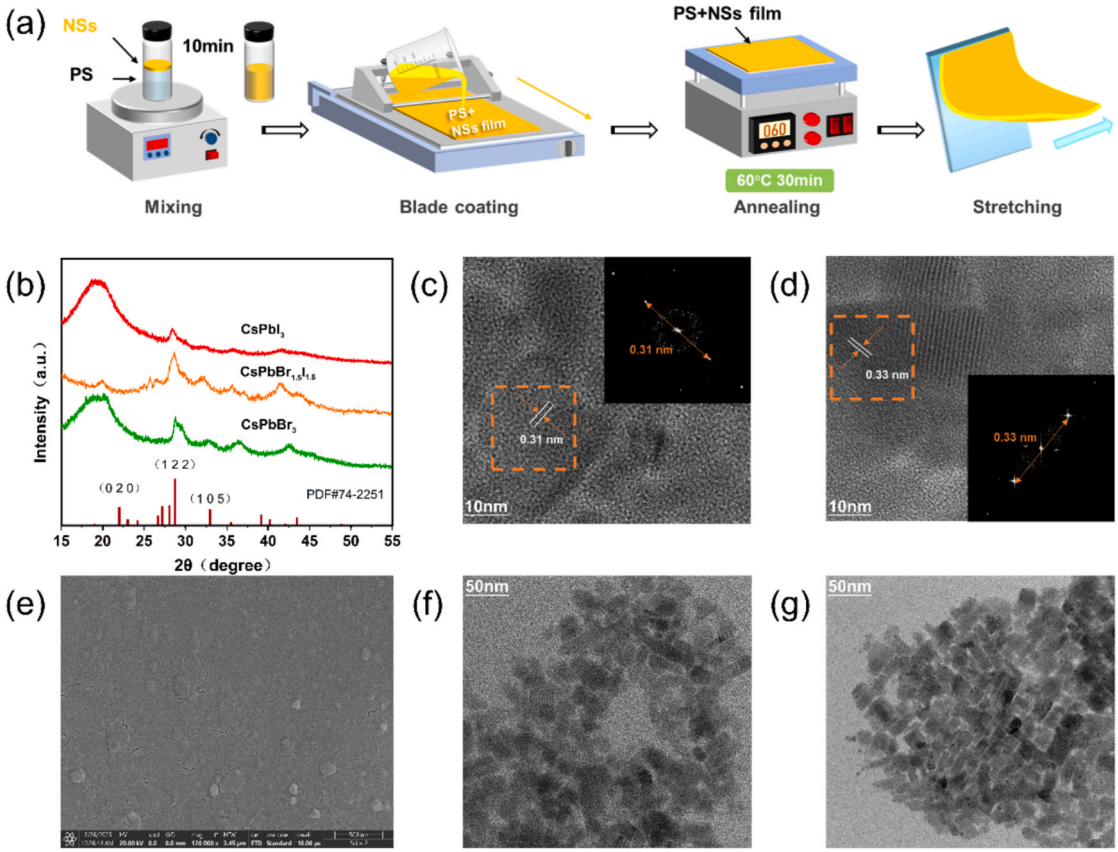

Fig. 1. (a) Process flow for the preparation of perovskite NS−PS composite films. (b) XRD patterns of the $CsPbBr_3$, $CsPbBr_{1.5}I_{1.5}$, and $CsPbI_3$ NS polymers. HRTEM images of (c) $CsPbBr_3$ and (d) $CsPbI_3$ NSs. (e) SEM image of the $CsPbBr_3$ NS polymer film. TEM images of (f) $CsPbBr_3$ and (g) $CsPbI_3$ NSs.

3.2. Luminescence properties of $CsPbX_3$ NS polymer films

Figs. 2a and b show the PL (under 380 nm UV laser excitation) and RL (X-ray excitation) spectra of the perovskite NSs encapsulated within the PS polymer. The peak emission wavelength of the $CsPbX_3$ NSs exhibited a clear dependence on the composition modulation achieved by varying the Br/I ratio. Intermediate compositions with systematically varying Br/I ratios exhibited tunable emissions across the visible spectrum (521–678 nm), demonstrating precise bandgap engineering via halide alloying. For instance, the $CsPbBr_3$ NSs exhibted an RL emission maximum at 521 nm, whereas the $CsPbI_3$ NSs exhibited a corresponding RL peak at 674 nm. This tunability, which could be governed by the compositional modulation of the crystalline lattice and electronic structure, confirmed the absence of phase segregation and highlighted the versatility of the material for wavelength-specific optoelectronics.

The PL spectra showed peaks that were blue-shifted by approximately 3–4 nm relative to the corresponding RL bands. Due to differences in the quantum confinement effects among nanosheets of varying sizes, changes in bandgap and emission wavelength occur, leading to spectral broadening and an increase in the full width at half maximum (FWHM) of the luminescence spectrum. This effect becomes more pronounced under X-ray excitation (Fig. 2a and b), which is consistent with the TEM results (Fig. 1f and g) [34]. Disordered halide alloys cause spectral broadening due to local potential fluctuations from the random

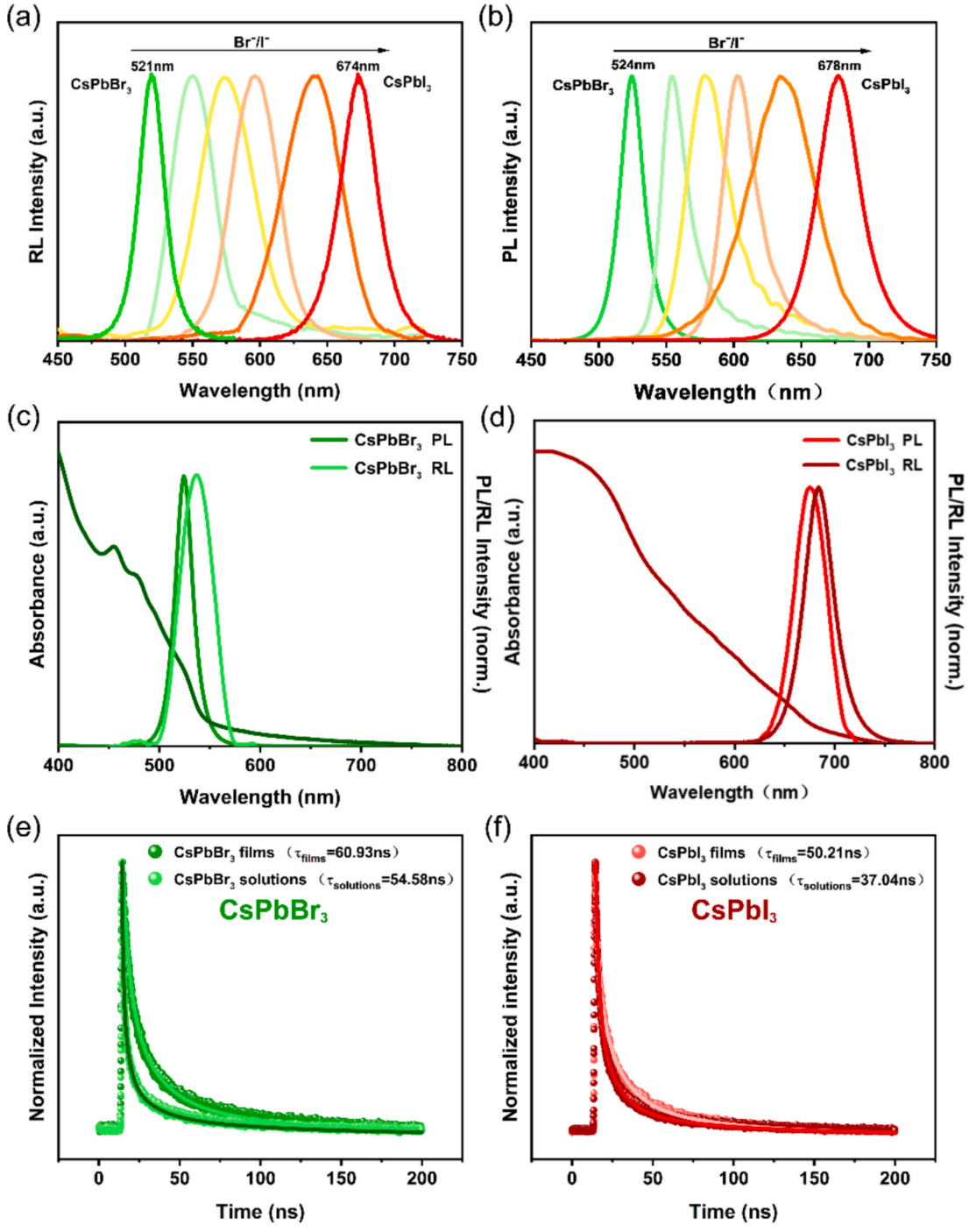

Fig. 2. (a) RL and (b) PL spectra of the $CsPbBr_{3-x}I_x$ NS polymer films at different halogen ratios. PL, RL, and absorption spectra of the (c) $CsPbBr_3$ and (d) $CsPbI_3$ NSs. Steady-state luminescence lifetimes of (e) $CsPbBr_3$ and (f) $CsPbI_3$ films and solutions.

Br^-/I^- distribution. In addition, variations in defect-state density create supplementary radiative recombination channels that further widen the emission spectrum [35,36]. Consequently, the interplay of these mechanisms leads to the observed broadening of the PL spectrum. The X-ray-induced RL spectra displayed notably broader FWHM values than the PL spectra. Although the spectral broadening in RL originates from factors such as disordered halide alloys and variations in defect-state density, this broadened emission profile serendipitously offers practical advantages for X-ray scintillation applications. The wider spectral profile improves the overlap integral with the detector's spectral response function, mitigating local variations in responsivity and enhancing the stability of the photoelectric conversion across the emission band. Furthermore, the broadened emission spectrum reduces optical coupling losses at the scintillator-detector interface by creating a more diffuse source. This is a key factor for maximizing the overall light yield and thereby enhancing the sensitivity of the polarization response. The resultant expansion in spectral coverage offers special advantages for X-ray scintillation applications, as it improves the spectral matching with response detectors and reduces optical coupling losses, which are key factors in enhancing the polarization response sensitivity. Further optimization of the halide ratios and defect engineering could achieve a better balance between the emission wavelength, bandwidth, and light yield. Spectroscopic analysis revealed that the emission peaks at distinct excitation wavelengths (520 nm for $CsPbBr_3$ and 677 nm for $CsPbI_3$) demonstrated the optoelectronic stability of these materials. The consistent 10 nm Stokes shift between the PL and RL emissions reflects the inherent radiative recombination mechanism in the perovskite systems. In addition, the photoluminescence quantum yield (PLQY) of $CsPbBr_3$ is 87.3 %, and 69.7 % for $CsPbI_3$.

Moreover, the $CsPbX_3$ NSs demonstrated composition-dependent polarized emission across the entire visible spectrum (521–678 nm). Fig. S3 presents the detailed performance metrics, including the PL/RL intensity spectra under varying X-ray tube voltages and UV laser powers. The PL intensity exhibited superlinear growth above a threshold power density of 30 mW/cm^2, which could be attributed to trap-state saturation and the dominant bimolecular recombination at high carrier densities. Conversely, the RL spectra displayed notable broadening (with the FWHM increasing by 25–40 % compared to PL) owing to polychromatic energy deposition and enhanced electron–phonon coupling. Additionally, the RL intensity exhibited a sublinear dependence on the dose rate ($I \propto P^{0.7}$), indicating Auger quenching and thermal dissipation effects at elevated excitation levels. This divergent response highlights the potential of this material for dual-mode UV/X-ray sensors, whereas RL broadening improves spectral matching with a polarization-sensitive response. As shown in Fig. 2c and d, both the PL and RL emission peaks maintained their spectral fidelity under UV/X-ray excitations. This reproducible shift confirmed the reliability of the energy transfer and recombination processes, which are crucial for polarization-sensitive responses.

Composition-dependent surface passivation significantly influences light transmission. Further investigation of the optical behavior of these perovskite NS films revealed enhanced radiative lifetimes in the NS films (Fig. 2e and f), particularly for $CsPbI_3$, which is indicative of more efficient radiative recombination processes. This likely contributes to the increased emission intensity compared to that of their colloidal counterparts. The prolonged lifetimes indicate that the excited carriers undergo radiative recombination more frequently than nonradiative decay, resulting in stronger emission signals. Quantitative analysis revealed a 6.35 ns lifetime enhancement for the $CsPbBr_3$ NS films (τ_{film} = 60.93 ns) compared to the solution-phase nanostructures ($\tau_{solution}$ = 54.58 ns). Notably, this lifetime extension was more pronounced in the $CsPbI_3$ systems, where the solid-state films exhibited a 13.17 ns increase (τ_{film} = 50.21 ns vs. $\tau_{solution}$ = 37.04 ns), indicating composition-dependent surface passivation effects.

For the $CsPbBr_3$ films, the moderate increase in lifetime suggested partial surface-state passivation, potentially causing light scattering or absorption at the interfaces, while preserving spectral fidelity through effective internal transmission pathways. For the $CsPbI_3$ films, a pronounced lifetime extension indicated superior surface passivation quality, enabling smoother light transmission channels within the film. The reduced density of non-radiative traps minimizes optical scattering and absorption, thereby enhancing photon propagation and subsequent luminescent emission. The extended radiative lifetime and preserved spectral features collectively demonstrate a microstructure conducive to efficient light transmission, where the perovskite NS structure facilitate photon propagation while minimizing optical losses. The observed spectral red-shift is attributed to the high carrier injection conditions under X-ray excitation. This process generates a high density of electron–hole pairs, saturating band-edge states and enhancing radiative recombination through lower-energy defect states. Deep-level defects below the conduction band dominate the radiative recombination process, favored by their higher occupation probability and slower carrier capture dynamics. Consequently, RL emission shifts to longer wavelengths compared to PL, which originates mainly from near-band-edge transitions. This consistent behavior highlights the key role of defect-mediated luminescence under high excitation in metal halide perovskite nanosystems [37,38].

3.3. Polarized luminescence performance of $CsPbX_3$ NS polymer films

The anisotropic two-dimensional morphology and unidirectional alignment of the $CsPbX_3$ NSs in the composite films imparted exceptional polarization-dependent optical properties. Polarized PL and RL measurements employing X-ray and UV laser excitation were conducted following the setup shown in Fig. 3a. By rotating a 400–700-nm broadband linear polarizer in the response detection path, the angle-dependent polarized emission could be systematically investigated. The polarizer obtained one result at 10-degree intervals, and 36 results were measured over a full revolution to obtain a polarization spectrum. The normalized angle-dependent emission characteristics, presented as polar plot representations in Fig. 3b, reveal pronounced anisotropy. The emission intensity peaks parallel to the principal orientation of the NSs and the minima perpendicular to it indicate considerable polarization modulation of the emission process, which can be attributed to the anisotropic optical transition dipole moments of the NSs.

The degree of polarization (DOP) can be calculated using the following standard formula:

$$\mathrm{DOP} = \frac{I_{max} - I_{min}}{I_{max} + I_{min}} \quad (1)$$

where I_{max} and I_{min} denote the maximum and minimum emission intensities measured along the orthogonal axes. To systematically investigate the correlation between halide composition and polarization behavior, a series of $CsPbBr_3$ NS composite films with controlled Br/I ratios were fabricated. The DOP values of the six samples with varying halogen ratios were measured using X-ray and UV laser excitations. Fig. 3c shows that the DOP values increased from 0.24 to 0.39 with the gradual doping of I^-, highlighting the critical role of iodide incorporation in enhancing the polarization characteristics of $CsPbX_3$ perovskites.

The larger atomic radius of I^- (2.20 Å) compared to that of Br^- (1.96 Å) induces lattice distortion, disrupting the cubic perovskite structure. This distortion breaks the spatial inversion symmetry, thereby enhancing the excitonic transition polarization selectivity. Asymmetric crystal fields promote anisotropic exciton recombination, which is directly correlated with the observed polarization enhancement in this study. Moreover, the narrower bandgap of $CsPbI_3$ (1.73 eV) compared to that of $CsPbBr_3$ (2.30 eV) contributes to a reduced exciton binding energy and extended exciton lifetime, enabling polarization-dependent exciton dynamics control during film formation [2]. These factors synergistically enhance the alignment of anisotropic excitonic dipoles, as reflected by the increasing DOP with I^- doping concentration. In

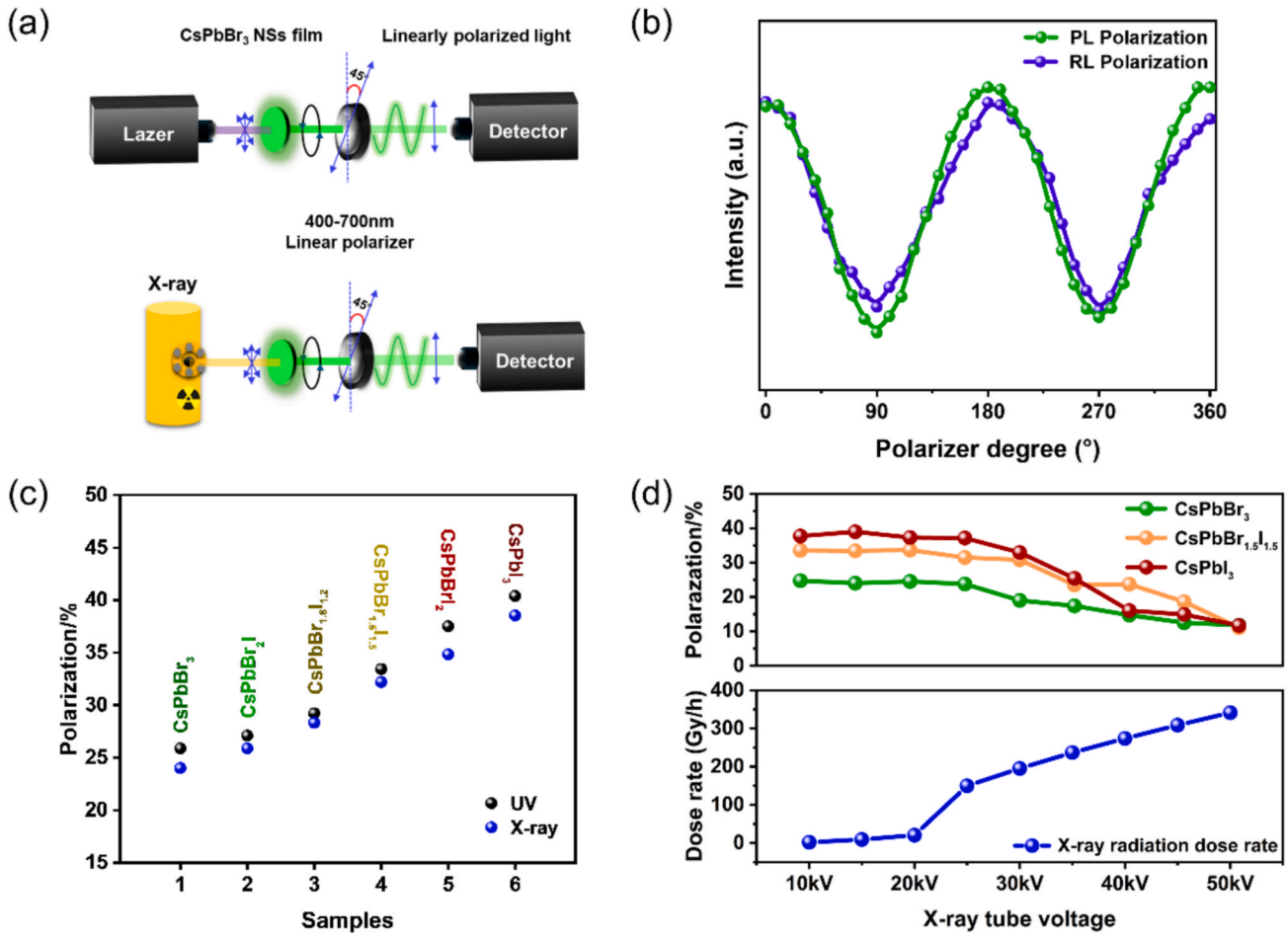

Fig. 3. (a) Setup used to measure the polarized PL and RL signals. (b) Polarization spectra of $CsPbBr_3$ under X-ray and UV laser excitation. (c) DOP of the $CsPbBr_{3-x}I_x$ NS polymer films with six different halogen ratios under X-ray and UV laser excitation. (d) Dose rate of X-rays and polarization of perovskite $CsPbX_3$ NSs under different X-ray tube voltages.

addition, in Fig. 3d, we provide a dependence curve on the polarization of the $CsPbX_3$ NSs to X-ray radiation dose, where the radiation dose range covers nine sets of data from 10 to 50 kV in the X-ray tube voltage for reference.

Current research indicates that individual nanoparticles outperform polymer-coated composite films in terms of their polarization characteristics [39,40]. Nevertheless, the nanoscale dimensions of discrete particles can hinder the observation of NS orientation changes and limit their application in solution-phase systems. Conversely, the NS-embedded composite films are more suitable for practical applications. Our analysis revealed that the polarization performance of the films strongly depended on their thickness. Regarding polymer matrix selection, comparative studies have demonstrated that PS-encapsulated $CsPbX_3$ maintains exceptional luminescence stability under severe conditions, such as long-term X-ray/UV irradiation and aqueous immersion. This performance advantage makes PS-based composites superior to conventional alternatives, such as PMMA-coated systems [41–43]. In this study, $CsPbI_3$ NS-PS composite films (0.2–1 mm) were fabricated by precisely controlling the blade gap thickness. Polarization-dependent PL and RL spectra (Fig. 4a and b) show that even with different excitation sources, films of different thicknesses exhibit similar curve variations, and the luminescence intensity increases to a certain extent with increasing film thickness. However, as the film thickness increased, the DOP of both materials under X-ray and UV excitation decreased (Fig. 4c), with a more significant decrease in the $CsPbBr_3$ NS-PS composite films being more obvious. This thickness-dependent depolarization arises from excessive NS stacking in thicker films, which disrupts the alignment. This deterioration is particularly evident in $CsPbBr_3$ films, where the polarization efficiency systematically decreases beyond their optimal thickness.

Conversely, ultra-thin films exhibit compromised polarization capabilities owing to their diminished PL/RL intensities and nonuniform NS distribution. The DOP values of the $CsPbBr_3$ NSs increased with progressive I^- doping under both excitation conditions, highlighting the role of iodide incorporation in enhancing polarization characteristics. However, the DOP values and their variation with halide composition differed between $CsPbBr_3$ and $CsPbI_3$, owing to the structural and bandgap differences. Moreover, individual nanoparticles exhibited superior polarization characteristics but were less practical than the NS-embedded composite films. PS-encapsulated $CsPbX_3$ exhibited better luminescence stability under various conditions than PMMA-coated systems.

Based on the above findings, the luminescence anisotropy in $CsPbX_3$ can be attributed to the synergistic effect of three interrelated factors: morphology, composition, and assembly. Although the perovskite possesses a macroscopically cubic crystal structure, its two-dimensional nanosheet morphology confines charge carriers predominantly in-plane and enhances out-of-plane quantum confinement, leading to direction-dependent optical behavior. Additionally, gradient iodine doping introduces lattice distortion due to the larger ionic radius of I^- compared to Br^-, breaking local symmetry and contributing to microstructural anisotropy. Finally, during film formation, shear-induced alignment of nanosheets in the polymer matrix creates ordered assemblies, manifesting as macroscopic optical anisotropy with distinct

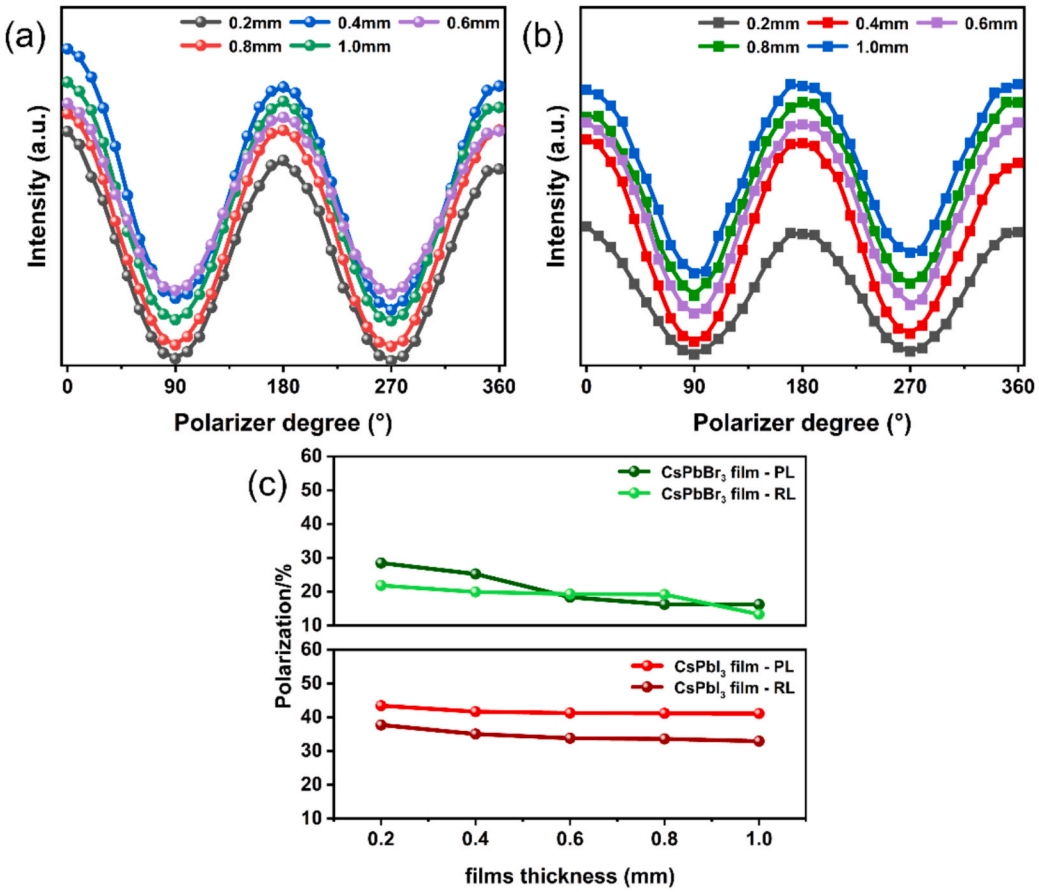

Fig. 4. Polarization spectra of (a) $CsPbBr_3$ and (b) $CsPbI_3$ NS polymer films with five different thicknesses ranging from 0.2 to 1.0 mm. (c) DOP value variations of the $CsPbBr_3$ and $CsPbI_3$ NS polymer films with five different thicknesses ranging from 0.2 to 1.0 mm under X-ray and 380 nm UV laser excitation.

luminescence intensities parallel and perpendicular to the alignment direction.

3.4. Application of $CsPbX_3$ NS films in polarization response

To evaluate the potential of $CsPbX_3$ NS composite films for practical UV polarization-response applications, we fabricated a polarization-response device for systematic characterization. As depicted in Fig. 5a, the device operates via a three-stage mechanism: (1) a laser source generates 380 nm UV radiation, which is linearly polarized using a polarizer (operational range: 400–700 nm); (2) this polarized UV excitation induces angle-dependent polarized PL emission from the NS composite films; and (3) a GaAs Photovoltaic module converts the emitted optical signals into electrical responses, quantified using a Keithley 2636A digital source meter. GaAs-based photovoltaic detectors were selected owing to their high EQE for the PL emission from $CsPbX_3$ materials, which aligned well with the emission spectra of $CsPbX_3$ and the EQE response range of detector [44]. The EQE was calculated from the photoresponsivity (R_λ) and incident wavelength (λ) as:

$$EQE(\%) = \frac{R_\lambda hc}{e\lambda} \quad (2)$$

Fig. 5b–d demonstrate that the $CsPbBr_3$ NS composite film exhibits a pronounced polarization-dependent photocurrent response across the 0–180° polarization axis. The characteristic relationship between the polarization angle and photocurrent intensity is shown in Fig. 5e–g. Analysis of the angle-dependent photoresponse revealed a maximum photocurrent at 0°, which gradually attenuated to a minimum at 90° before recovering to a maximum at 180°. This periodic modulation precisely aligns with the previous polarized PL and radiance spectral measurements. The angular of the dependence photocurrent fitted excellently to a sinusoidal function, confirming the intrinsic polarization sensitivity of the material.

Quantitative evaluation yielded polarization ratios (I_{max}/I_{min}) of 1.71, 2.04, and 4.12 for the $CsPbBr_3$, $CsPbBr_{1.5}I_{1.5}$, and $CsPbI_3$ NS composite films, respectively, based on the experimental data analysis (Fig. S4). The significantly higher polarization ratio observed for the $CsPbI_3$ NS composite film underscores the superior polarization sensitivity inherent to the $CsPbX_3$ NS composite architecture. These findings collectively highlight the unique advantages of $CsPbX_3$ nanomaterials for UV-polarized light detection applications [10,45]. Furthermore, the demonstrated polarization-sensitive photoresponse suggests the potential extension of $CsPbX_3$ NS composite films to X-ray-polarized photodetection. This prospect leverages the material's inherent anisotropic optoelectronic properties and reported radiation tolerance, potentially opening new avenues for advanced polarized radiation-sensing technologies.

4. Conclusion

In conclusion, we demonstrated pronounced polarization anisotropy in mixed-halide perovskite $CsPbX_3$ NSs. Their composite films exhibited exceptional polarization performance under X-ray and UV excitation, positioning them as ideal candidates for polarization-sensitive applications. Iodide doping systematically enhances the DOP of $CsPbBr_3$ NSs via synergistic lattice distortion and bandgap engineering, which is consistent with anisotropic excitonic dipoles. Notably, this study elucidates the mechanism of X-ray-induced linearly polarized luminescence in perovskite nanosheets, providing fundamental insights into their behavior under high-energy excitation. These findings establish $CsPbX_3$

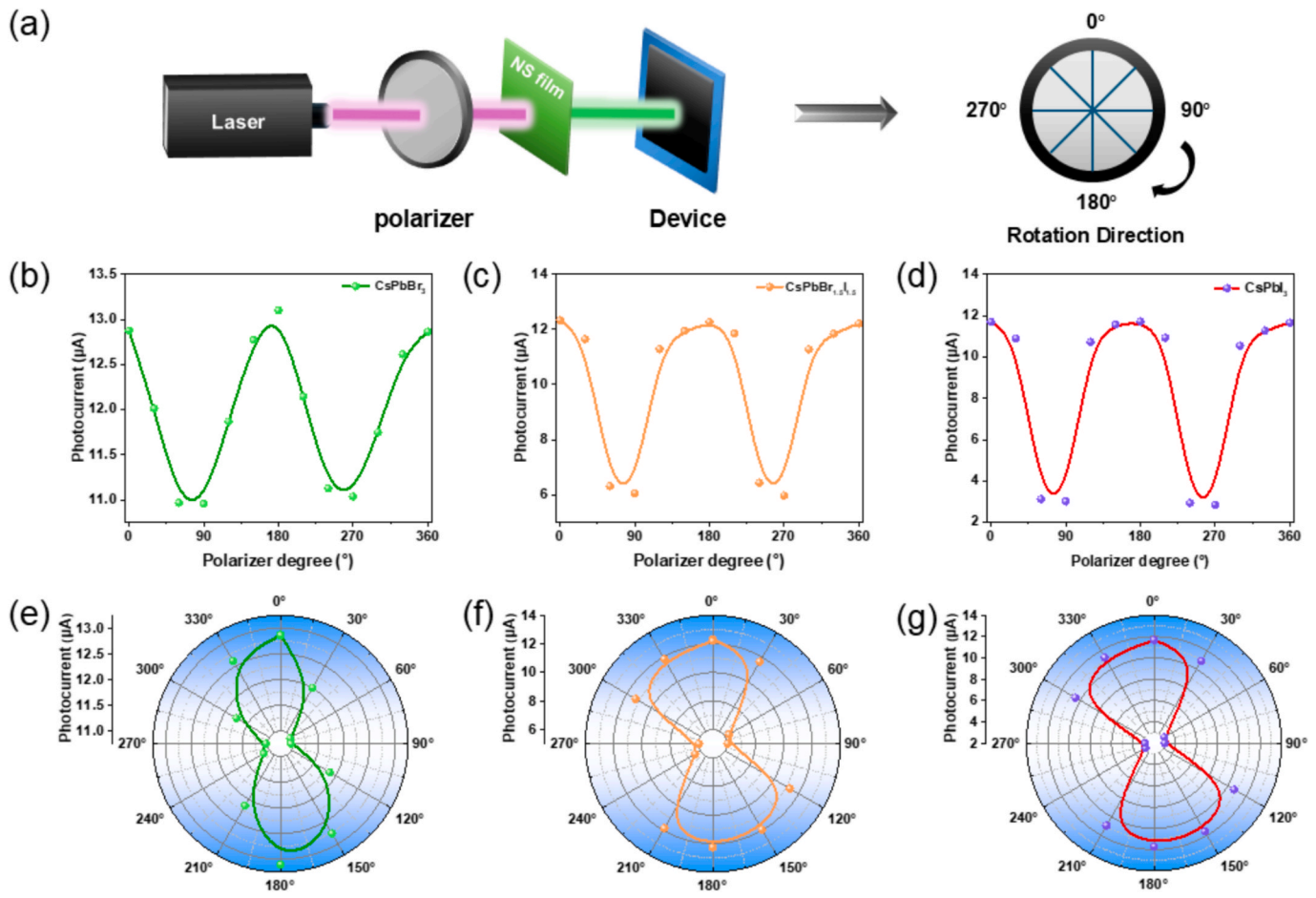

Fig. 5. (a) Setup used for the polarization response test. Polarization dependence of the polarization response of (b) $CsPbBr_3$, (c) $CsPbBr_{1.5}I_{1.5}$, and (d) $CsPbI_3$. Polar plots of the polarization response of (e) $CsPbBr_3$, (f) $CsPbBr_{1.5}I_{1.5}$, and (g) $CsPbI_3$.

NSs composites as promising materials for X-ray polarization-resolved detection.

CRediT authorship contribution statement

Zhibin Xu: Writing – original draft, Methodology, Formal analysis, Data curation. **Zhiheng Xu:** Writing – review & editing, Supervision, Funding acquisition, Conceptualization. **Sirui Zhu:** Writing – review & editing, Methodology, Investigation. **Xuebin Zhang:** Writing – review & editing, Visualization, Investigation. **Dandan Yang:** Writing – review & editing, Visualization, Formal analysis. **Xiaobin Tang:** Writing – review & editing, Supervision.

Declaration of competing interest

The authors declare that they have no known competing financial interests or personal relationships that could have appeared to influence the work reported in this paper.

Acknowledgments

This work was supported by the National Natural Science Foundation of China (Grant No. 12275132 and 62204215), and the Prospective Layout Project of Nanjing University of Aeronautics and Astronautics (Grant No. ILB240161A24). We acknowledge the Center for Microscopy and Analysis at Nanjing University of Aeronautics and Astronautics for the structural characterization of materials.

Appendix A. Supplementary data

Supplementary data to this article can be found online at https://doi.org/10.1016/j.apsusc.2025.165240.

Data availability

Data will be made available on request.

References

[1] Y. Fu, H. Zhu, C.C. Stoumpos, Q. Ding, J. Wang, M.G. Kanatzidis, X. Zhu, S. Jin, Broad wavelength tunable robust lasing from single-crystal nanowires of cesium lead halide perovskites ($CsPbX_3$, X= Cl, Br, I), ACS Nano 10 (8) (2016) 7963–7972.
[2] D. Wang, D. Wu, D. Dong, W. Chen, J. Hao, J. Qin, B. Xu, K. Wang, X. Sun, Polarized emission from $CsPbX_3$ perovskite quantum dots, Nanoscale 8 (22) (2016) 11565–11570.
[3] D. Zhang, Y. Yang, Y. Bekenstein, Y. Yu, N.A. Gibson, A.B. Wong, S.W. Eaton, N. Kornienko, Q. Kong, M. Lai, A.P. Alivisatos, S.R. Leone, P.J. Yang, Synthesis of composition tunable and highly luminescent cesium lead halide nanowires through anion-exchange reactions, J. Am. Chem. Soc. 138 (23) (2016) 7236–7239.
[4] I. Ali, J. Munir, Q. Ain, H.M. Ghaithan, A.S. Aldwayyan, A.A.A. Ahmed, S.M. H. Qaid, A spin-polarized DFT analysis of the physical attributes of vacancy ordered Rb_2TcCl_6 double perovskite for optoelectronic and spintronics, J. Magn. Magn. Mater. 601 (2024) 172180.
[5] Y. Chen, L. Tang, X. Zeng, W. Guo, T. Yang, H. Xu, Y. Liu, G. Gou, Y. Zhao, J. Luo, Z. Sun, Inch-size achiral perovskite single crystals for distinguishing circularly polarized light with a large asymmetry factor, Adv. Funct. Mater. 34 (17) (2024) 2311726.
[6] Q. Liu, P. Wang, Q. Wei, L. Zhou, H. Ren, C. Wang, J. Peng, L. Zhao, M. Li, Chiral perovskite nanowire optoelectronic synapse for full-stokes polarization-resolved perception and reservoir computing, Adv. Funct. Mater. 35 (8) (2025) 2415551.
[7] Y. Wang, X. Liu, Q. He, G. Chen, D. Xu, X. Chen, W. Zhao, J. Bao, X. Xu, J. Liu, X. Wang, Reversible transformation between CsPbBr 3 perovskite nanowires and

nanorods with polarized optoelectronic properties, Adv. Funct. Mater. 31 (22) (2021) 2011251.
[8] Y. Song, L. Li, M. Hao, W. Bi, A. Wang, Y. Kang, H. Li, X. Li, Y. Fang, D. Yang, Q. Dong, Elimination of interfacial-electrochemical-reaction-induced polarization in perovskite single crystals for ultrasensitive and stable X-ray detector arrays, Adv. Mater. 33 (52) (2021) 2103078.
[9] S. Li, G. Zhang, H. Xia, Y. Xu, C. Lv, H. Sun, Template-confined growth of Ruddlesden-Popper perovskite micro-wire arrays for stable polarized photodetectors, Nanoscale 11 (39) (2019) 18272–18281.
[10] Y. Zhou, J. Luo, Y. Zhao, C. Ge, C. Wang, L. Gao, C. Zhang, M. Hu, G. Niu, Tang, Flexible linearly polarized photodetectors based on all-inorganic perovskite $CsPbI_3$ nanowires, Adv. Opt. Mater. 6 (22) (2018) 1800679.
[11] J. Ye, A. Ren, L. Dai, T. Baikie, R. Guo, D. Pal, S. Gorgon, J.E. Heger, J. Huang, Y. Sun, R. Arul, G. Grimaldi, K. Zhang, J. Shamsi, Y.-T. Huang, H. Wang, J. Wu, A. F. Koenderink, L.T. Murciano, M. Schwartzkopf, S.V. Roth, P. Mueller-Buschbaum, J.J. Baumberg, S.D. Stranks, N.C. Greenham, L. Polavarapu, W. Zhang, A. Rao, R.L. Z. Hoye, Direct linearly polarized electroluminescence from perovskite nanoplatelet superlattices, Nat. Photonics 18 (6) (2016) 586–594.
[12] Z. Wen, R. Lu, K. Zheng, F. Gu, L. Zhang, H. Jin, Y. Chen, S. Wang, S. Pan, Enabling efficient blue-emissive circularly polarized luminescence by in situ crafting of chiral quasi-2D perovskite nanosheets within polymer nanofibers, Adv. Funct. Mater. 33 (7) (2023) 2212095.
[13] A. Hubley, A. Bensalah-Ledoux, B. Baguenard, S. Guy, B. Abecassis, B. Mahler, Chiral perovskite nanoplatelets exhibiting circularly polarized luminescence through ligand optimization, Adv. Opt. Mater. 10 (19) (2022) 2200394.
[14] W. Chen, S. Zhang, M. Zhou, T. Zhao, X. Qin, X. Liu, M. Liu, P. Duan, Two-photon absorption-based upconverted circularly polarized luminescence generated in chiral perovskite nanocrystals, J. Phys. Chem. Lett. 10 (12) (2019) 3290–3295.
[15] H. Chen, Y. Li, D. Xue, Perspective on perovskite materials as X-ray detectors, Sci. China Technol. Sci. 65 (2022) 244–246.
[16] C. Lin, K. Huang, Y. Chen, S. Hsueh, M. Li, P. Chen, Perovskite-based X-ray detectors, Nanomaterials 13 (13) (2023) 2024.
[17] Y. Su, W. Ma, Y.J. Yang, Perovskite semiconductors for direct X-ray detection and imaging, J. Semicond. 41 (5) (2020) 051204.
[18] F. Yao, K. Dong, W. Ke, G. Fang, Micro/nano perovskite materials for advanced X-ray detection and imaging, ACS Nano 18 (8) (2024) 6095–6110.
[19] R. Zhuang, X. Wang, W. Ma, Y. Wu, X. Chen, L. Tang, H. Zhu, J. Liu, L. Wu, W. Zhou, X. Liu, Y. Yang, Highly sensitive X-ray detector made of layered perovskite-like $(NH_4)_3Bi_2I_9$ single crystal with anisotropic response, Nat. Photonics 13 (9) (2019) 602–608.
[20] M.P. Davydova, L. Meng, M.I. Rakhmanova, Z. Jia, A.S. Berezin, I.Y. Bagryanskaya, Q. Lin, H. Meng, A.V. Artem'ev, Strong magnetically-responsive circularly polarized phosphorescence and X-ray scintillation in ultrarobust Mn (II)–organic helical chains, Adv. Mater. 35 (35) (2023) 2303611.
[21] D. Wu, J. Wei, B. Luo, L. Zhou, P. Chen, J. Tian, J. Pan, A.V. Emeline, J.Z. Zhang, Q. Pang, Circularly polarized luminescence in achiral Tin-based perovskites via structural Isomer-driven coordination interaction, J. Phys. Chem. Lett. 16 (17) (2025) 4181–4188.
[22] L. Yang, Z. Zhang, R. Wang, M. Qiu, Y. Wang, M. Li, S. Huang, Z. Wu, L. He, X. Dai, Z. Chai, S. Wang, Y. Wang, Design of a high-performance near-infrared scintillator through metal-atom substitution in metal chalcogenide, Inorg. Chem. 48 (2024) 22656–22661.
[23] X. Niu, H. Lu, B. Zhang, T. Shao, Y. Zhang, H. Wang, Z. Wang, T. Qiao, W. Zhao, B. Sun, Y. Xie, Z. Chang, S. Lai, H. Zhang, G. Long, Chiral terbium halide for narrow-band X-ray scintillation, Nano Lett. 25 (39) (2025) 14420–14426.
[24] Z. Zhou, T. Jiang, Y. Yang, Y. Deng, M. Wang, Y. Ma, S. Liu, Q. Zhao, Multifunctional chiral five-coordinated manganese (II) complexes for white led and X-ray imaging applications, Adv. Opt. Mater. 12 (7) (2024) 2302185.
[25] K.J. Babu, G. Kaur, L. Biswal, G. De, H.N. Ghosh, Ultrafast charge delocalization dynamics of ambient stable $CsPbBr_3$ nanocrystals encapsulated in polystyrene fiber, Chem Eur J 27 (2) (2021) 683–691.
[26] H. Min, W. Jung, J. Yang, H.S. Oh, B.J. Yoo, W.J. Moon, H. Kim, H.J. Lee, Systematic approach to the study of optical stability according to the crystal structure of perovskite quantum dots, J. Phys. Chem. C 127 (46) (2023) 22713–22720.
[27] X. Tang, Z. Zu, Z. Zang, Z. Hu, W. Hu, Z. Yao, W. Chen, S. Li, S. Han, M. Zhou, $CsPbBr_3$/reduced graphene oxide nanocomposites and their enhanced photoelectric detection application, Sens. Actuators B Chem. 245 (2017) 435–440.
[28] Y. Zhang, Y. Huang, C. Zhou, Y. Xu, J. Zhong, H. Mao, Crystalline structures and optoelectronic properties of orthorhombic $CsPbBr_3$ polycrystalline films grown by the Co-evaporation method, Vacuum 202 (2022) 111219.
[29] B. Chaudhary, Y.K. Kshetri, H.S. Kim, S.W. Lee, T.H. Kim, Current status on synthesis, properties and applications of $CsPbX_3$ (X= Cl, Br, I) perovskite quantum dots/nanocrystals, Nanotechnology 32 (50) (2021) 502007.
[30] S. Singh, M. Singh, M. Arora, D. Singh, S.P. Singh, J. Indian, Uncertainty measurements in chemically synthesized stable uniform sized gold nanoparticles for TEM/HRTEM calibration, Indian J. Pure Appl. Phys. 59 (2) (2021) 83–91.
[31] X. Zhu, Z. Zhang, Y. Mao, Y. Li, X. Huang, N. Gu, Applying deep learning in automatic and rapid measurement of lattice spacings in HRTEM images, Sci. China Mater. 63 (11) (2020) 2365–2370.
[32] D. Yang, X. Zhang, Y. Yang, Z. Xu, S. Liu, K. Cheng, S. Guo, Q. Xu, S. Jeon, L. Li, H. Zeng, Revealing the self-assembly behavior of $CsPbBr_3$ nanoscale supercrystals mediated by packed clusters, ACS Mater. Lett. 6 (4) (2024) 1439–1446.
[33] D. Liang, Z. Xu, D. Yang, Z. Xu, W. Yin, X. Tang, Ultra-stable $CsPbBr_3$-embedded polymer films for spectrally tunable X-ray nuclear batteries and flexible radiation imaging applications, J. Mater. Chem. C 12 (42) (2024) 17115–17121.
[34] A.S. Abbas, D. Chabeda, D. Weinberg, D.T. Limmer, E. Rabani, A. Paul Alivisatos, Non-monotonic size-dependent exciton radiative lifetime in $CsPbBr_3$ nanocrystals, Nat. Commun. 16 (1) (2025) 6401.
[35] Y. Wang, X. Guan, W. Chen, J. Yang, L. Hu, J. Yang, S. Li, K. Kalantar-Zadeh, X. Wen, T. Wu, Illumination-induced phase segregation and suppressed solubility limit in Br-rich mixed-halide inorganic perovskites, ACS Appl. Mater. Interfaces 12 (34) (2020) 38376–38385.
[36] Z. Zaaboub, F. Hassen, H. Maaref, Kinetic of recombination processes involving defect-related states in as-grown Si-doped GaAsN/GaAs epilayer, Solid State Commun. 314 (2020) 113913.
[37] C. Qiu, Y. Song, H.X. Deng, S.H. Wei, Dual-level enhanced nonradiative carrier recombination in wide-gap semiconductors: the case of oxygen vacancy in SiO_2, J. Am. Chem. Soc. 145 (45) (2023) 24952–24957.
[38] J. Chen, J. Wang, X. Xu, J. Li, J. Song, S. Lan, S. Liu, B. Cai, B. Han, J.T. Precht, H. Zeng, Efficient and bright white light-emitting diodes based on single-layer heterophase halide perovskites, Nat. Photonics 15 (3) (2021) 238–244.
[39] T. Guner, G. Topcu, U. Savaci, A. Genc, S. Turan, E. Sari, M.M. Demir, Polarized emission from $CsPbBr_3$ nanowire embedded-electrospun PU fibers, Nanotechnology 29 (13) (2018) 135202.
[40] J. Wang, Y. Zhang, J. Chen, Y. Wei, D. Yu, L. Liang, Y. Liu, Y. Wu, W. Shen, X. Li, H. Zeng, Strong polarized photoluminescence $CsPbBr_3$ nanowire composite films for UV spectral conversion polarization photodetector enhancement, ACS Appl. Mater. Interfaces 13 (30) (2021) 36147–36156.
[41] L. Chen, C. Tien, Z. Tseng, Y. Dong, S. Yang, Influence of PMMA on all-inorganic halide perovskite $CsPbBr_3$ quantum dots combined with polymer matrix, Materials 12 (6) (2019) 985.
[42] Y. Shen, X. Yan, S. Ni, H. Zhang, H. Liu, X. Yang, Ag-$CsPbBr_3$ quantum dots/PMMA composite film for tunable white light emitting diodes, Mater. Lett. 304 (2021) 130691.
[43] B. Shu, Y. Chang, S. Yang, L. Dong, J. Zhang, X. Cheng, D. Yu, Fabrication and optical properties of high-quality blue-emitting $CsPbBr_3$ QDs-PMMA films, Opt. Mater. 115 (2021) 111069.
[44] Z. Xu, X. Tang, Y. Liu, Z. Zhang, W. Chen, K. Liu, Z. Yuan, $CsPbBr_3$ quantum dot films with high luminescence efficiency and irradiation stability for radioluminescent nuclear battery application, ACS Appl. Mater. Interfaces 11 (15) (2019) 14191–14199.
[45] S.X. Li, G.P. Zhang, H. Xia, Y.S. Xu, C. Lv, H.B. Sun, Template-confined growth of Ruddlesden–Popper perovskite micro-wire arrays for stable polarized photodetectors, Nanoscale 11 (39) (2019) 18272–18281.